

Supporting Information

***D-p* orbital hybridization in RhSn catalyst boosts hydrogen oxidation reaction under alkaline electrolyte**

Lixin Su, Yuanmeng Zhao, Yiming Jin, Xinran Fan, Zeyu Liu and Wei Luo*

EXPERIMENTAL SECTION

Chemicals and Materials.

Rhodium (III) acetylacetonate ($\text{Rh}(\text{acac})_3$, Changcheng Chemical, > 99%), tin (II) acetate ($\text{Sn}(\text{Ac})_2$, Shanghai D&B Biological Science and Technology, 98%), oleylamine (OAm, Aladdin Industrial, 80 ~ 90%), hexane (Sinopharm Chemical Reagent, $\geq 97\%$), absolute ethanol (Sinopharm Chemical Reagent, $\geq 99.7\%$), sulfuric acid (H_2SO_4 , Sinopharm Chemical Reagent, 95.0 ~ 98.0%), copper (II) sulfate pentahydrate ($\text{CuSO}_4 \cdot 5\text{H}_2\text{O}$, Sinopharm Chemical Reagent, $\geq 99.0\%$), potassium hydroxide (KOH, Aladdin Industrial, 99.999% metals basis, except sodium), isopropanol (Sinopharm Chemical Reagent, $\geq 99.7\%$), Nafion® 117 solution (Sigma-Aldrich, ~ 5% in a mixture of lower aliphatic alcohols and water), and Pt/C (Johnson Matthey Hispec 3600, Shanghai Hesen Electric, 20%) were used directly without any further treatment. The ultrapure water ($18.25 \text{ M}\Omega \text{ cm}^{-1}$) prepared from an up water purification system (Ulupure) was used throughout the whole experiment.

Synthesis of RhSn and Rh.

Typically, OAm (6.0 mL), Sn(Ac)₂ (12.0 mg) and Rh(acac)₃ (60.0 mg) were added to a three-neck flask and stirred magnetically. Subsequently, temperature of solution was increased to 100 °C and kept for 30 min under vacuum to remove the moisture and oxygen in the reaction system. After the solution was refilled with nitrogen, and the temperature was further raised to 300 °C and maintained at this temperature for 60 min. The resulting solution was cooled to room temperature naturally. Subsequently, RhSn samples were collected by centrifugation with adding n-hexane and ethanol and dried at room temperature under vacuum. Besides, the syntheses of RhSn samples with other Sn proportions are same as the above synthesis, excepting for the different Sn(Ac)₂ amount of 8.0 and 16.0 mg. In addition, Rh sample was synthesized via above same procedure without adding Sn(Ac)₂.

Synthesis of RhSn/C and Rh/C.

The as-prepared samples and XC-72 carbon were dispersed into hexane and ethanol solution in a three-neck flask via sonication for 30 min. After stirring overnight under the nitrogen, the resulting samples were collected by centrifugation with adding n-hexane and dried at room temperature under vacuum. Finally, the dried samples were put in a quartz boat in the center of a tube furnace and annealed under a gas atmosphere (5% H₂, 95% N₂) at 400 °C for 60 min. The temperature of tube furnace was raised at a rate of 5 °C min⁻¹.

Synthesis of RhGa/C and RuSn/C.

The syntheses of RhGa/C and RuSn/C are similar with that of RhSn/C, excepting for the amount of Ga(acac)₃ (18.5 mg), Sn(Ac)₂ (12.0 mg) and Ru(acac)₃ (60.0 mg).

Materials characterization.

The X-ray powder diffraction (XRD) patterns were obtained on a Rigaku Miniflex600 X-ray powder diffractometer equipped with a Cu K α radiation source ($\lambda = 0.154178$ nm). All of the diffraction data were collected in a 2θ range from 20° to 80° at a scanning rate of 8° min^{-1} . The transmission electron microscopy (TEM) observation and the energy dispersive spectroscopy (EDS) data were performed using a FEI Tecnai G20 U-Twin transmission electron microscope equipped with an EDX spectrometer at an acceleration voltage of 200 kV. High resolution TEM (HRTEM) images and high angle annular dark field scanning transmission electron microscopy (HAADF-STEM) images were conducted on a Titan G2 60-300 transmission electron microscope operated at an acceleration voltage of 300 kV. X-ray photoelectron spectroscopy (XPS) measurement was performed with a Kratos XSAM 800 spectrophotometer. Inductively coupled plasma atomic emission spectroscopy (ICP-AES) was performed on a Thermo IRIS Intrepid II XSP atomic emission spectrometer.

Preparation of working electrodes.

For hydrogen oxidation reaction (HOR), 4.0 mg of RhSn/C, Rh/C, or commercial Pt/C was mixed with 2.0 mL of isopropanol solvent containing 0.05 wt% Nafion and ultrasonicated for 30 min to form a homogeneous ink. The glassy carbon (GC) electrode with a diameter of 5 mm was polished with 0.05 mm gamma alumina powder slurry,

and rinsed with ultrapure water and ethanol to obtain a neat surface. When the GC electrode was dried under air naturally, 5.0 μL ink was drop-casted on the surface of the GC electrode and dried in air before any electrochemical measurements. Compared with HOR, the preparation for the working electrode of hydrogen evolution reaction (HER) only differed in the loading. 5.0 mg catalyst powders were mixed with 1.0 mL of isopropanol solvent containing 0.1 wt% Nafion and 6.0 μL ink was drop-casted on the surface of the GC electrode.

Electrochemical measurements.

Electrochemical tests were conducted at CHI 760E electrochemistry workstation. The GC electrode decorated by electrocatalyst served as the working electrode, and the graphite rod served as the counter electrode as well as the saturated calomel electrode (SCE) or the Hg/HgO electrode was used as reference electrode. In this study, all operation was performed at the constant temperature at 303 (\pm 0.1) K, and all the measured potentials were referred to the reversible hydrogen electrode (RHE) potential with iR -compensation. For HOR evaluation, the catalysts were pre-treated under Ar-saturated 0.1 M KOH by cyclic voltammetry (CV) curves from \sim 0.02 to 1.12 V for RhSn/C, Rh/C and Pt/C samples to obtain a stable voltammogram. After the fresh electrolyte was H₂-saturated, the polarization curve was performed in the potential range from about -0.08 to 0.92 V for these samples at a scan rate of 10 mV s⁻¹ under the RDE rotation rate of 1600 rpm. For HER, the catalysts were pre-treated under Ar-saturated 0.1 M KOH by cyclic voltammetry (CV) curves to obtain a stable

voltammogram. Then, the polarization curve was recorded by a rotating disk electrode (RDE) system (Pine Research Instruments) with the rotation rate of 1600 revolutions per minute (rpm) at a scan rate of 5 mV s^{-1} in Ar-saturated 0.1 M KOH . Accelerated durability test (ADT) was operated by 1000 CV cycles under Ar-saturated electrolyte for both HER and HOR. As for the ADT of HOR, the precious metal loading toward RhSn/C is 4.292 ug .

Electrochemically active surface areas (ECSAs) were tested by Cu underpotential deposition (Cu_{UPD}) stripping. Typically, CV on each catalyst was first carried out at a scan rate of 10 mV s^{-1} in Ar-purged $0.1 \text{ M H}_2\text{SO}_4$ solution to obtain a steady voltammogram as the background. Then, Cu_{UPD} stripping was performed at a scan rate of 10 mV s^{-1} in Ar-purged $0.1 \text{ M H}_2\text{SO}_4$ solution containing 2 mM CuSO_4 after Cu deposition at about 0.30 V for 100 s , with the potential beginning from about 0.30 V . The value of ECSA (cm^2) can be calculated by Eq. S1,

$$ECSA = \frac{Q_{Cu}}{Q_s} \quad \text{Eq. S1}$$

Where Q_{Cu} is the measured integral charge, Q_s is the surface charge density of $420 \mu\text{C cm}_{\text{metal}}^{-2}$ which is assumed for a monolayer adsorption of Cu_{UPD} on metal.

Electrochemical impedance spectra (EIS) tests were conducted with the AC impedance spectra from 200 kHz to 0.1 kHz and a voltage perturbation of 10 mV . The real part of the resistance at 1 kHz was taken as the uncompensated resistance (R_u) and was used to obtain the iR -free potential ($E_{iR\text{-free}}$) according to the following equation (Eq. S2),

$$E_{iR-free} = E - iR_u \quad \text{Eq. S2}$$

where E is the measured potential and i is the corresponding current.

Nernstian diffusion overpotential (η_{diff}) could be calculated from Eq. S3,

$$\eta_{diff} = -\frac{RT}{nF} \left(1 - \frac{j}{j^d} \right) \quad \text{Eq. S3}$$

where R , T , F , n , and j^d are the universal gas constant ($8.314 \text{ J mol}^{-1} \text{ K}^{-1}$), the temperature in Kelvin (303 K), the Faraday constant, the electron transfer number, and the hydrogen diffusion limited current density, respectively.

Kinetic current density (j^k) could be deduced from the Koutecky-Levich equation (Eq. S4),

$$\frac{1}{j} = \frac{1}{j^k} + \frac{1}{j^d} = \frac{1}{j^k} + \frac{1}{Bc_0\omega^{1/2}} \quad \text{Eq. S4}$$

where j , B , c_0 , and ω are the measured current density, the Levich constant, the solubility of H_2 ($7.33 \times 10^{-4} \text{ mol L}^{-1}$), and the speed of the rotating, respectively.

Exchange current density (j^0) could be extracted from the Butler-Volmer equation (Eq. S5),

$$j^k = j^0 \left[e^{\frac{\alpha F}{RT} \eta} - e^{-\frac{(1-\alpha)F}{RT} \eta} \right] \quad \text{Eq. S5}$$

j^0 could be also obtained from the approximate Butler-Volmer equation (Eq. S6),

$$j = j^0 \frac{\eta F}{RT} \quad \text{Eq. S6}$$

where α and η represent the transfer coefficient and the overpotential, respectively.

CO-tolerance test was performed using the same electrochemical measurements of HOR test. The long-term stability tests were performed using chronoamperometry conducted in 0.1 M KOH saturated with CO containing (100 ppm) H₂ and measured at 0.05 V for more than 1 h. Before and after stability test, the linear sweep voltammetry (LSV) curves were carried out in 0.1 M KOH saturated with H₂ at the rotation rate of 1600 rpm and the potential was ranged from -0.08 V to 0.92 V at a scan rate of 10 mV·s⁻¹.

CO stripping was conducted by keeping the electrode potential at 0.1 V for 10 min in 0.1 M KOH solution with 99.99% CO for CO adsorbed on metal surface, followed by Ar purging for another 30 min to remove residual CO in the electrolyte. The CO stripping current was obtained via CV in a potential region from 0 to 1.1 V at a sweep rate of 20 mV s⁻¹.

DFT calculations.

Periodic DFT calculations with a plane-wave basis set were performed. The generalized gradient approximation functional of the Perdew-Burke-Ernzerhof (PBE) form was used to describe the exchange and correlation interactions.¹ Ultrasoft pseudopotential was adopted to treat the interactions between ionic cores and valence electrons.² The electronic wave functions were expanded on a plane wave basis with a cut-off energy

of 400 eV. The optimization convergence criterion was set as 1×10^{-5} eV in energy and 0.01 eV/Å in force, respectively. The Brillouin zone was sampled by the MonkhorstPack scheme with a $4 \times 4 \times 1$ k-points mesh for all of the surfaces. The Rh and RhSn (111) surfaces were chose for calculations. The adsorption free energies were determined by the following formula $\Delta G = \Delta E + \Delta ZPE - T\Delta S$, where ΔE , ΔZPE and ΔS represent the binding energy, zero point energy change and entropy change of the adsorption of adsorbates, respectively. The related zero point energies and entropies of H_2 , H_2O , H^* and OH^* are from previous literatures.^{3,4}

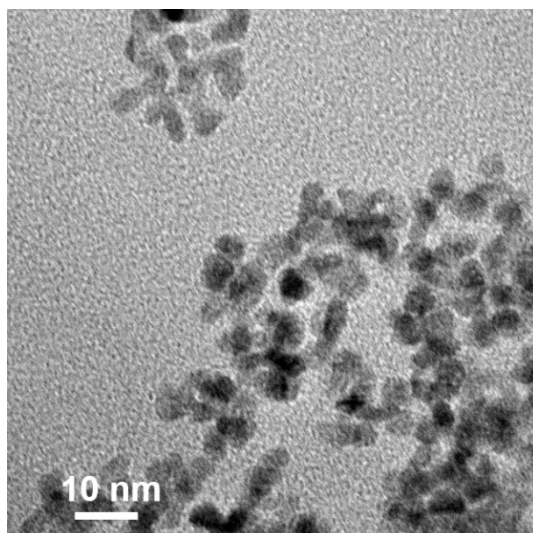


Figure S1. TEM image of Rh.

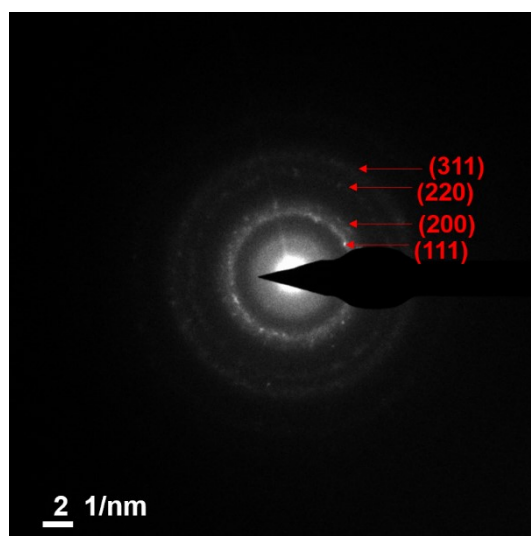


Figure S2. SAED pattern of RhSn/C.

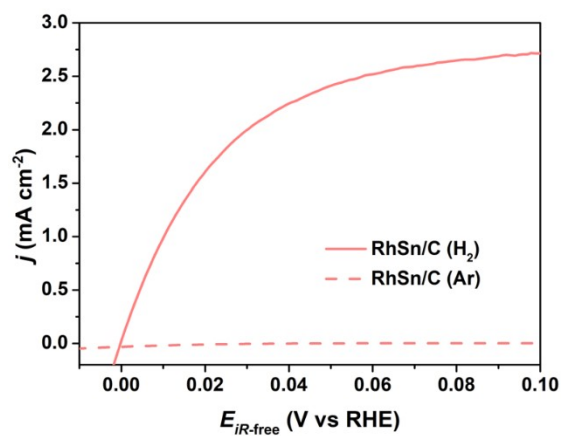


Figure S3. Comparison of polarization curves of RhSn/C recorded in H₂-saturated 0.1 M KOH and Ar-saturated 0.1 M KOH.

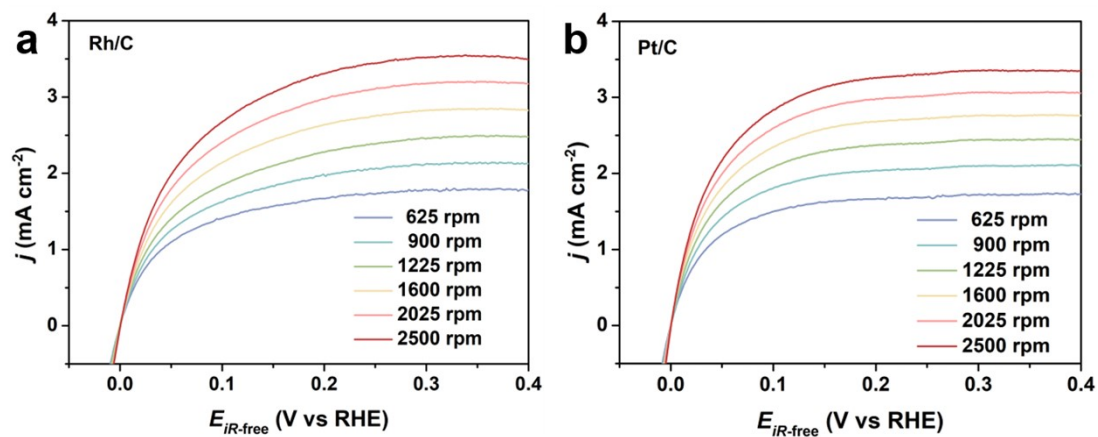


Figure S4. HOR polarization curves in H₂-saturated 0.1 M KOH with a scanning rate of 10 mV s⁻¹ at the rotating rates ranging from 2500 rpm to 625 rpm of Rh/C (a) and Pt/C (b).

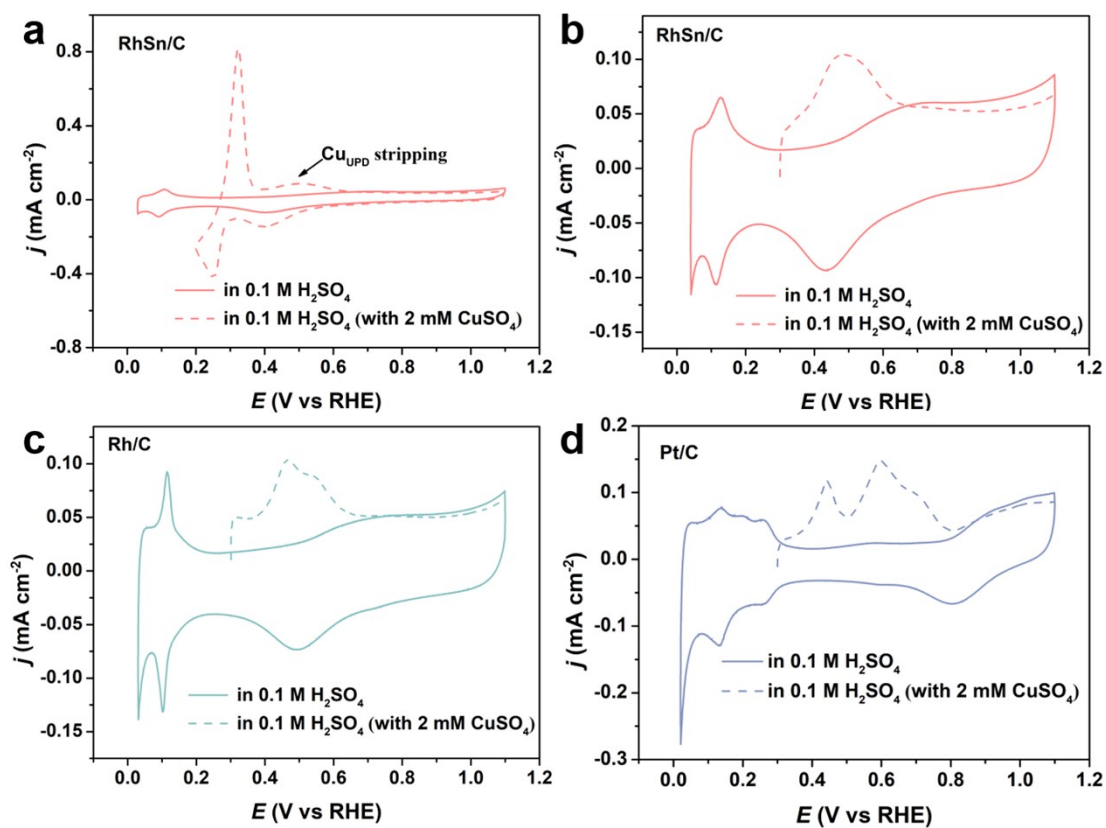


Figure S5. (a) CVs of RhSn/C in Ar-saturated 0.1 M H₂SO₄ with or without 2 mM CuSO₄ at a scan rate of 10 mV s⁻¹. The anodic peak (arrow) corresponds to Cu_{UPD} peak. CVs (solid lines) and Cu_{UPD} stripping voltammograms (dash lines) of (b) RhSn/C, (c) Rh/C and (d) Pt/C.

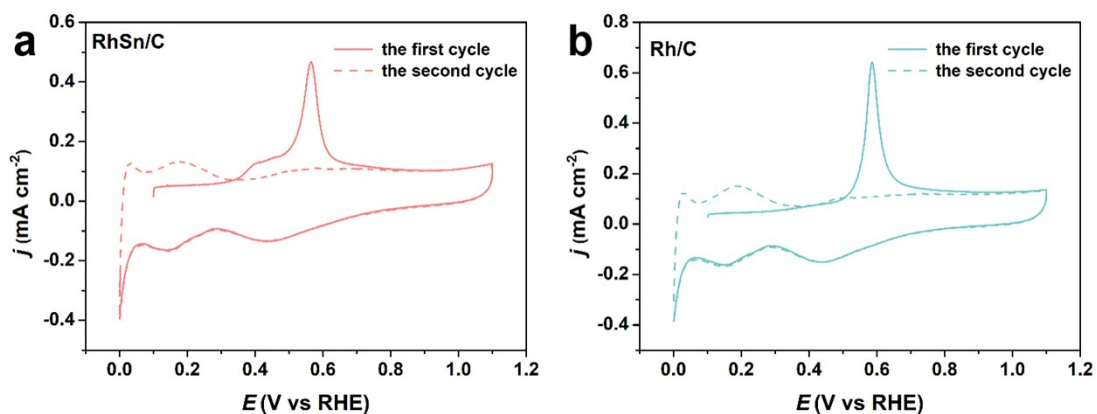


Figure S6. CO stripping curves in CO-saturated 0.1 M KOH at a scan rate of 20 mV s⁻¹ towards RhSn/C (a) and Rh/C (b). The dashed curves show the second cycle of the measurements.

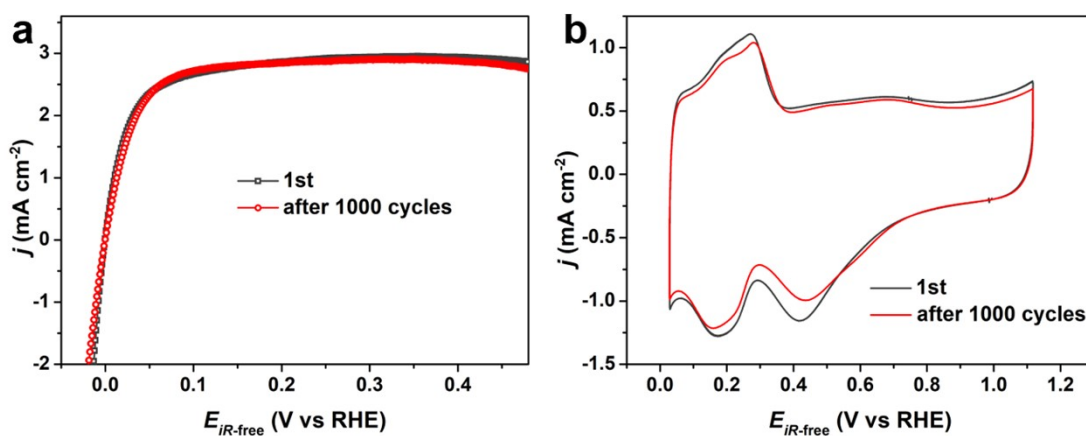


Figure S7. HOR polarization curves (a) and CV curves (b) of RhSn/C recorded before and after 1000 CV cycles in 0.1 M KOH (ADT of HOR).

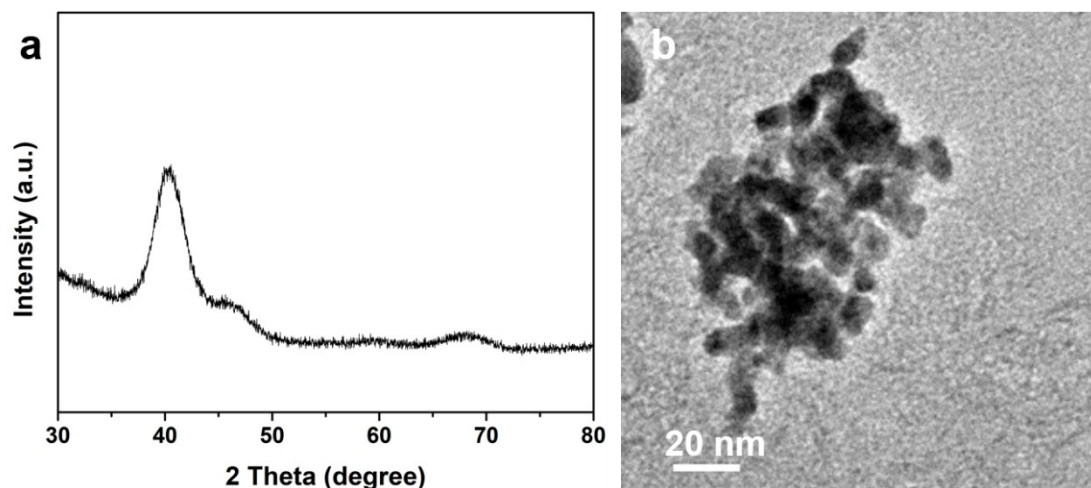


Figure S8. (a) XRD pattern and (b) TEM image toward RhSn/C after ADT of HOR.

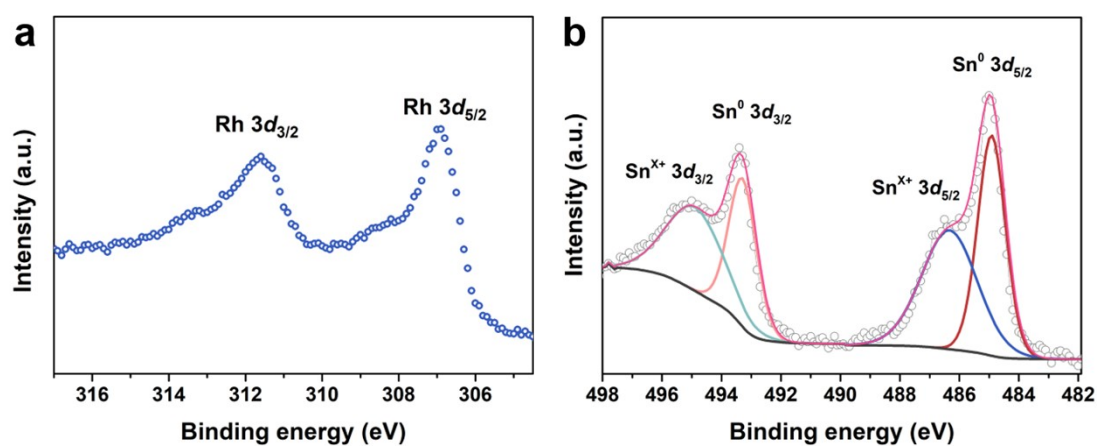


Figure S9. High resolution XPS of (a) Rh 3d and (b) Sn 3d in RhSn/C after ADT of HOR.

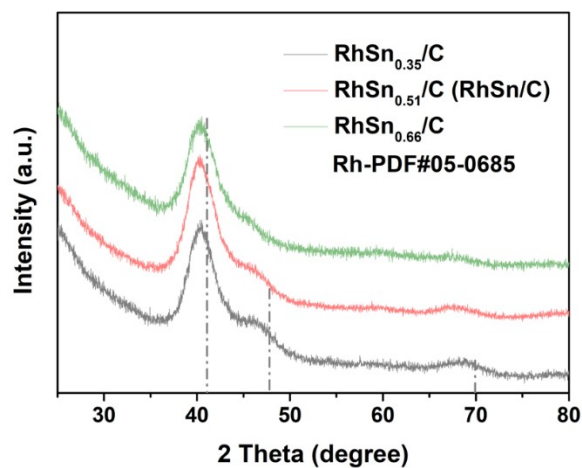


Figure R10. XRD patterns of RhSn_{0.35}/C, RhSn_{0.51}/C (RhSn/C) and RhSn_{0.66}/C.

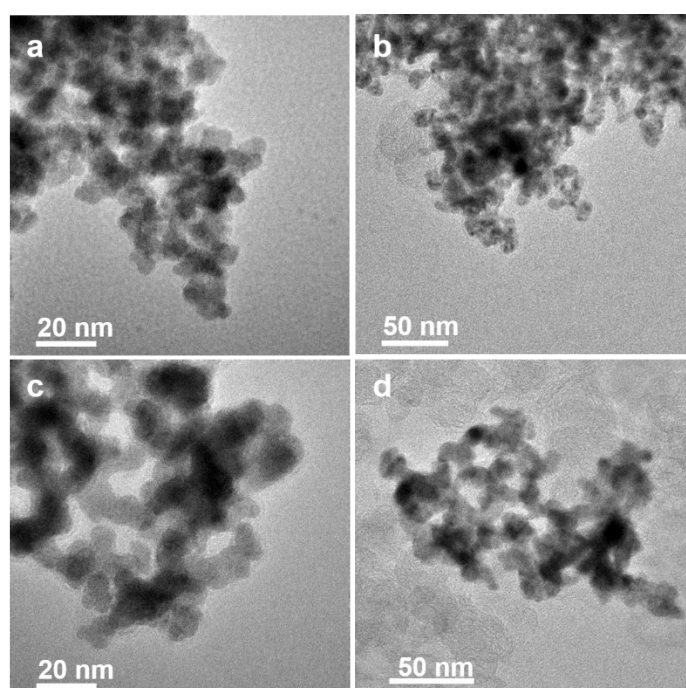


Figure R11. TEM images of RhSn_{0.35} (a), RhSn_{0.35}/C (b), RhSn_{0.66} (c) and RhSn_{0.66}/C

(d).

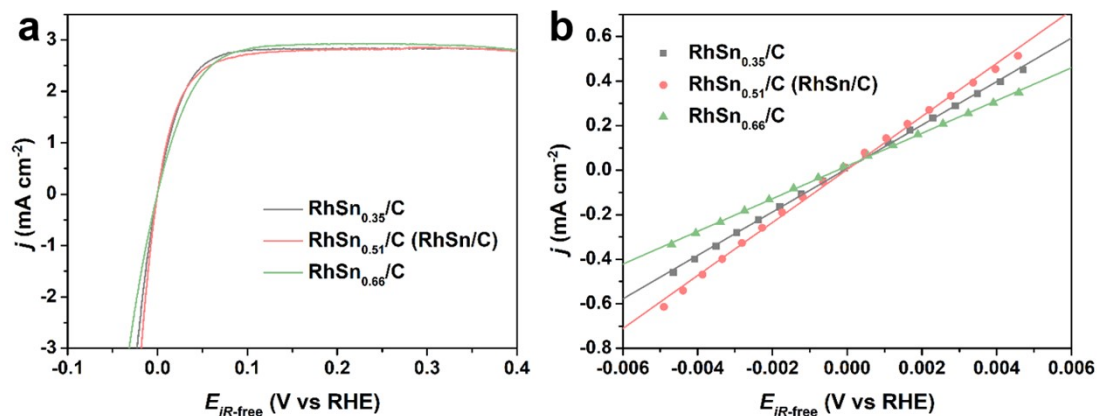


Figure R12. (a) HOR polarization curves in H₂-saturated 0.1 M KOH at a rotating speed of 1600 rpm, (b) Linear fitting curves in the micro-polarization region of RhSn_{0.35}/C, RhSn_{0.51}/C (RhSn/C) and RhSn_{0.66}/C.

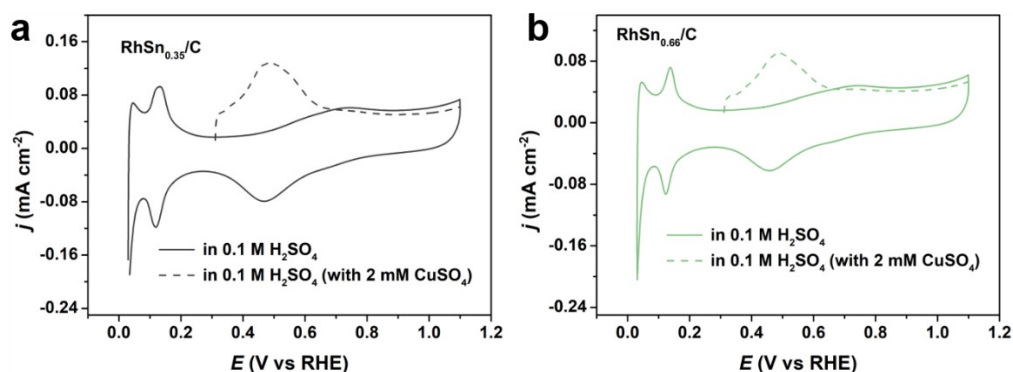


Figure R13. CVs (solid lines) and Cu_{UPD} stripping voltammograms (dash lines) of (a) RhSn_{0.35}/C and (b) RhSn_{0.66}/C.

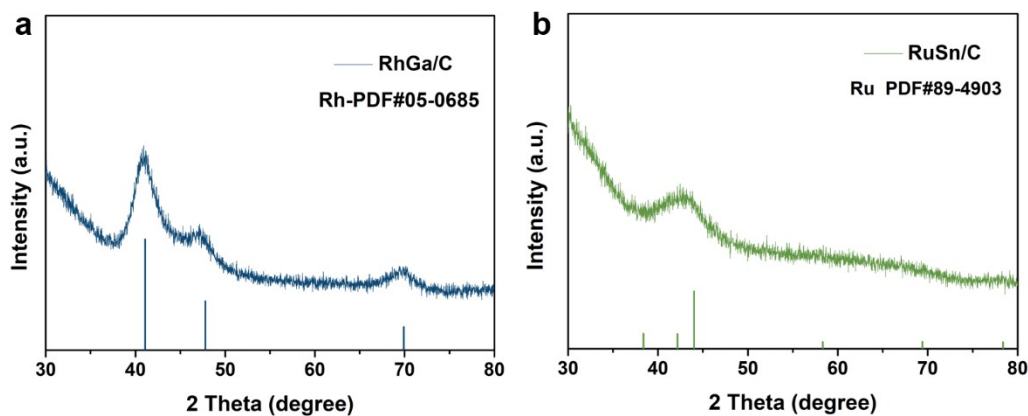


Figure R14. XRD patterns of RhGa/C (a) and RuSn/C (b).

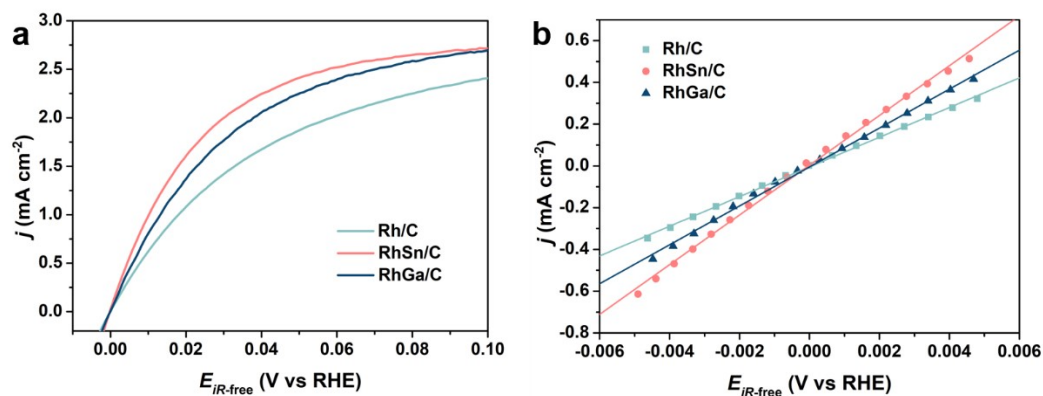


Figure R15. (a) HOR polarization curves in H₂-saturated 0.1 M KOH at a rotating

speed of 1600 rpm, (b) Linear fitting curves in the micro-polarization region of Rh/C, RhSn/C and RhGa/C.

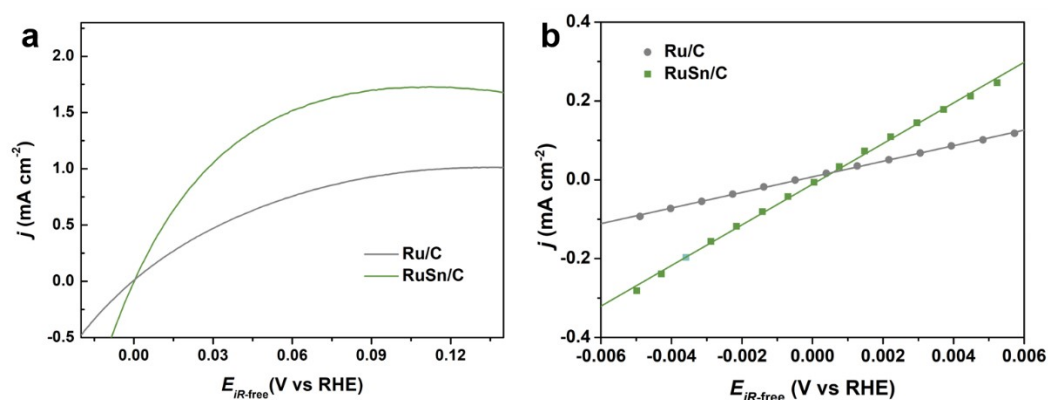


Figure R16. (a) HOR polarization curves in H₂-saturated 0.1 M KOH at a rotating speed of 1600 rpm, (b) Linear fitting curves in the micro-polarization region of Ru/C and RuSn/C.

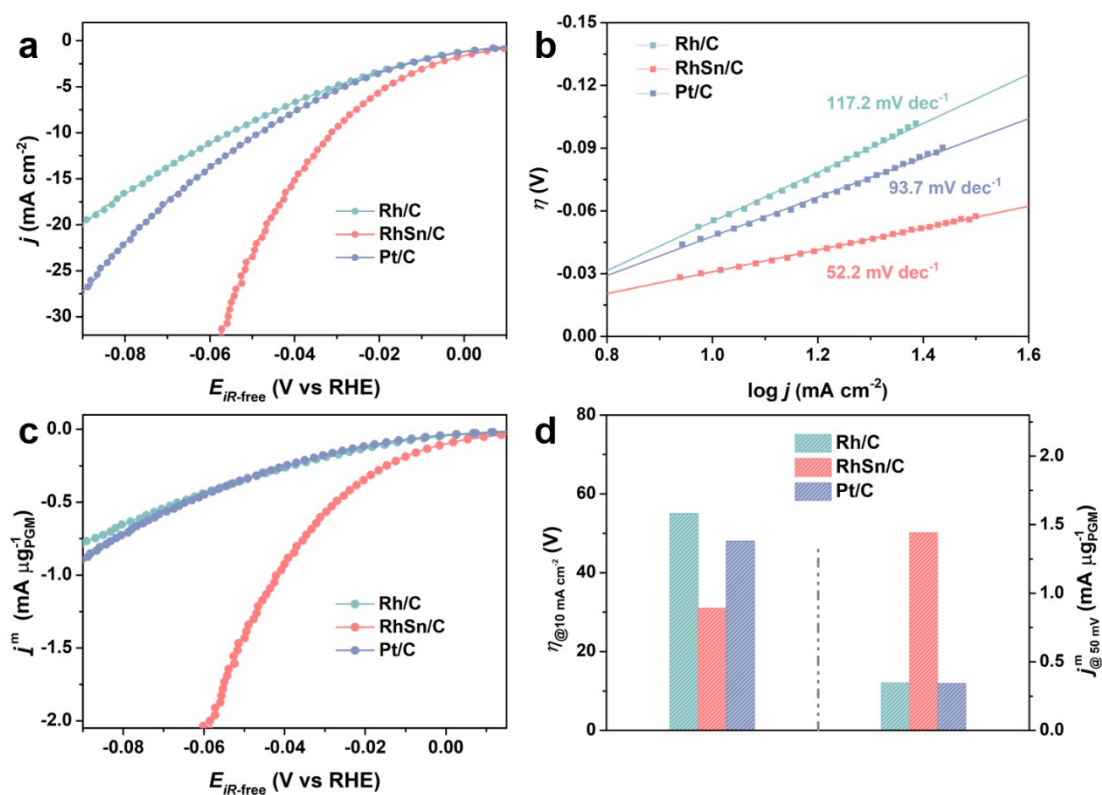


Figure S17. (a) HER polarization curves in Ar-saturated 1.0 M KOH at a scan rate of

5 mV s^{-1} with a rotation speed of 1600 rpm, (b) Tafel plots, (c) The polarization curves (a) normalized by the precious metal loadings, (d) Overpotentials at the current density of 10 mA cm^{-2} and the mass activities at the overpotential of 50 mV towards Rh/C, RhSn/C and commercial Pt/C.

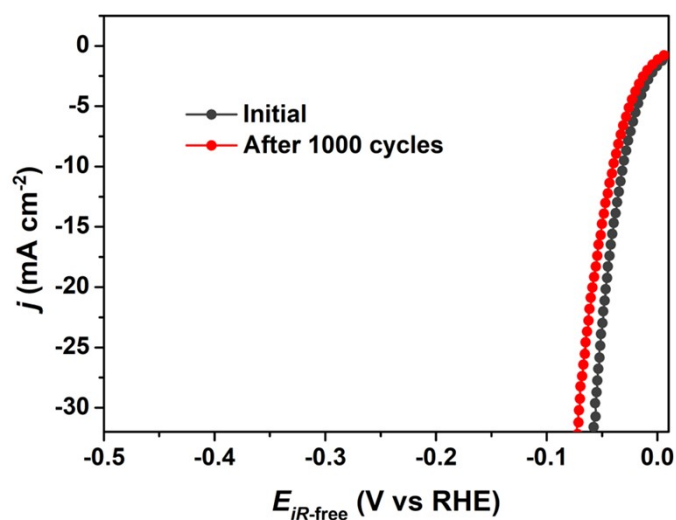


Figure S18. HER polarization curves of RhSn/C recorded before and after 1000 CV cycles in 0.1 M KOH (after ADT of HER).

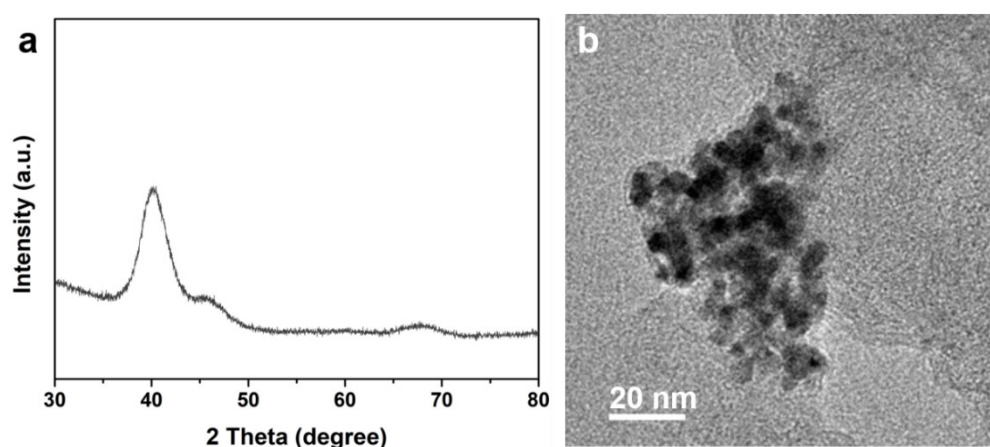


Figure S19. (a) XRD pattern and (b) TEM image toward RhSn/C after ADT of HER.

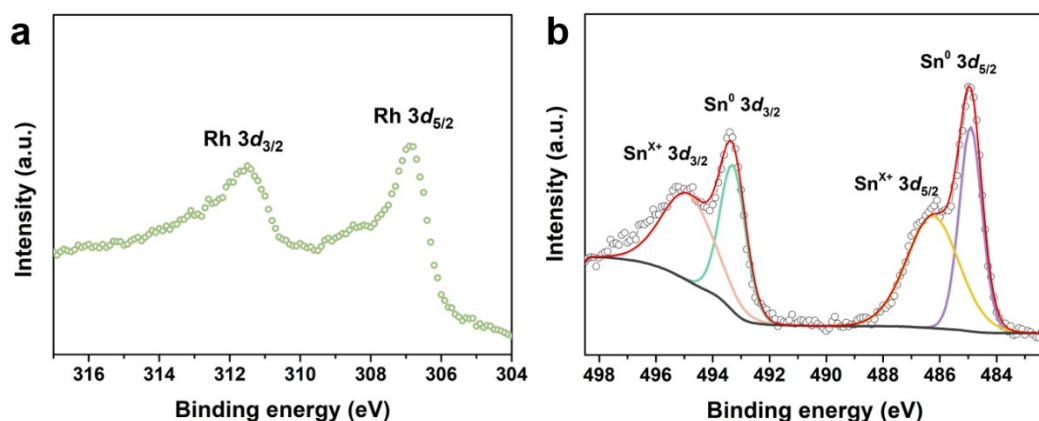


Figure S20. High resolution XPS of (a) Rh 3d and (b) Sn 3d in RhSn/C after ADT of HER.

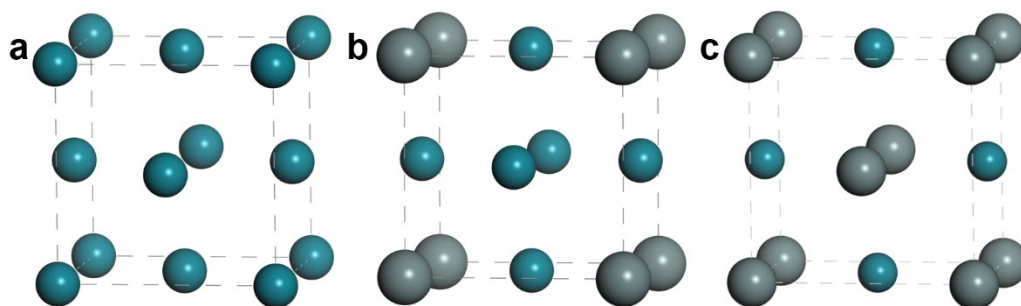


Figure S21. The crystal structure of (a) Rh unit cell, (b) RhSn (Rh : Sn = 3 : 1) unit cell (the representative structure in main text for other calculation) and (c) RhSn (Rh : Sn = 1 : 1) unit cell after fully relaxed. Dark cyan and caesious balls represent rhodium and tin atoms, respectively.

Based on the ICP results, the metal ratios of Rh/Sn in the as-prepared RhSn catalysts were from 1/0.35 to 1/0.66, and the proportion of the catalytic interface might fluctuate in certain small zones. Given that the surface of DFT calculated models might not completely coincide with the catalytic interface of RhSn, we selected a scale range for DFT calculation which the Rh and Sn composition of as-prepared RhSn catalysts were among them. Meanwhile, the Rh and RhSn catalysts are *fcc* structure and the number of molecules in the unit cell (*Z*) is 4. Thus, we conducted the crystal parameter of DFT calculated models with atomic ratios of Rh and Sn from 3/1 to 1/1 (2/2).

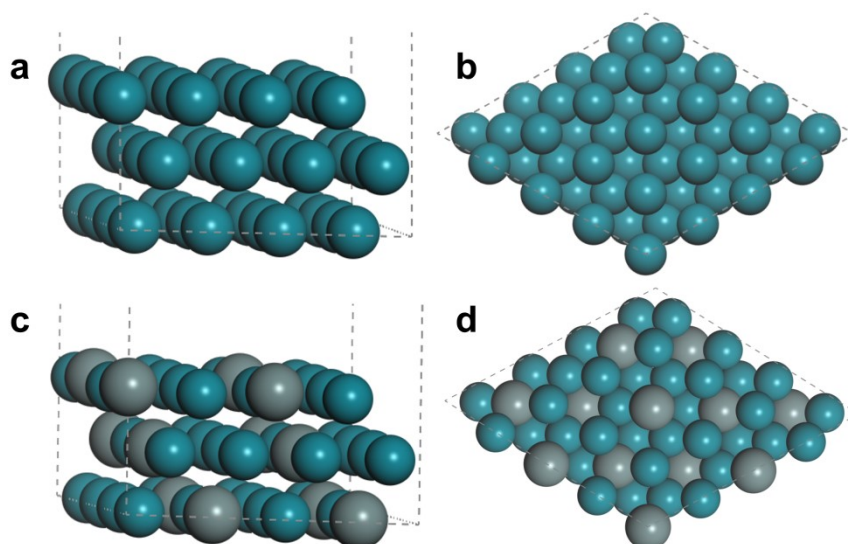


Figure S22. The side view (a) and top view (b) for Rh (111) surface. The side view (c) and top view (d) for RhSn (111) surface.

The (111) plane is chosen for calculation based on the following reasons. First of all, the (111) plane is the most exposed and stable surface towards RhSn/C and Rh/C catalysts as confirmed from XRD patterns and HRTEM image. Besides, numerous related literatures have confirmed that the interfacial free energy (γ) of *fcc* structure follows: $\gamma\{111\} < \gamma\{100\} < \gamma\{110\}$, indicating the nanocrystals always incline to expose the $\{111\}$ facets to minimize the total surface energy.

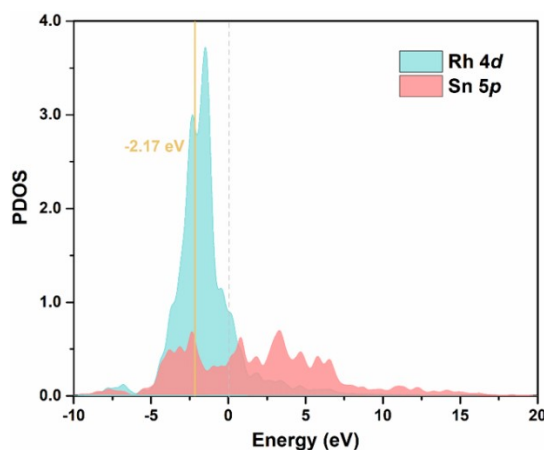


Figure S23. The *d*-PDOS of Rh and *p*-PDOS of Sn in RhSn (Rh : Sn = 1 : 1).

It can be seen unambiguously that Rh 4*d*-PDOS and Sn 5*p*-PDOS is also matched well in RhSn (Rh : Sn = 1 : 1) model, indicating the RhSn featuring the *d-p* orbital hybridization. Notably, the *d*-band centers of RhSn (Rh : Sn = 1 : 1) (-2.17 eV) and RhSn (Rh : Sn = 3 : 1) (-2.22 eV) are much closer to Fermi energy, compared to pure Rh (-2.57 eV), derived from the different degree of *d-p* orbital hybridization, leading to

stronger adsorption towards adsorbates, such as OH*. Thus, it can be concluded that the strengthened OHBE for RhSn catalysts with different proportions of Sn, revealed by their different positions of *d*-band center, are responsible for their enhanced activities, in comparison to the Rh/C.

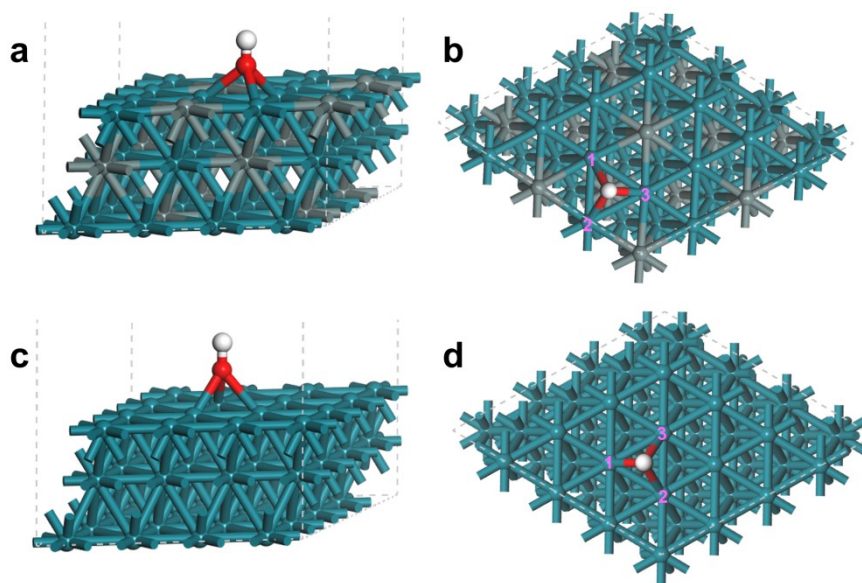


Figure S24. The side view (a) and top view (b) for OH on RhSn (111) surface. The side view (c) and top view (d) for OH on Rh (111) surface. Dark cyan, caesious, red and white balls represent rhodium, tin, oxygen and hydrogen atoms, respectively.

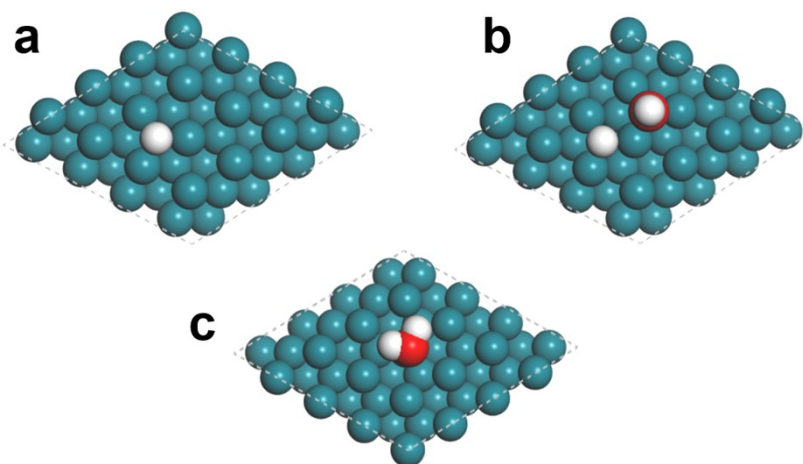


Figure S25. The optimized structure models of the adopted adsorption sites of H, H-OH and H₂O (a, b and c) on the surface of Rh.

Table S1. ICP-AES data of Rh/C, RhSn_{0.35}/C, RhSn_{0.51}/C (RhSn/C) and RhSn_{0.66}/C.

Sample	Rh (wt%)	Sn (wt%)
Rh/C	16.59	/
RhSn _{0.35} /C	12.09	4.92
RhSn _{0.51} /C (RhSn/C)	10.73	6.31
RhSn _{0.66} /C	9.86	7.52

Table S2. The HOR activities of catalysts in this work.

Sample	Butler-Volmer fitting			Micropolarization		
	α	$j^{0,s}$ (mA cm _{ECSA} ⁻²)	$j^{0,m}$ (mA μg _{PGM} ⁻¹)	$j^{k,m}_{@10mV}$ (mA μg _{PGM} ⁻¹)	$j^{0,s}$ (mA cm _{ECSA} ⁻²)	$j^{0,m}$ (mA μg _{PGM} ⁻¹)
Rh/C	0.597	0.532	0.244	0.099	0.489	0.216
RhSn/C	0.769	0.933	0.590	0.246	0.852	0.509
Pt/C	0.752	0.318	0.218	0.109	0.310	0.214

Table S3. Comparison of the HOR activity in 0.1 M KOH for catalysts in this work with other precious metal-based catalysts reported.

Catalysts	$j^{0,s}$ (mA cm _{ECSA} ⁻²)	$j^{0,m}$ (mA μg _{Pt} ⁻¹)	References
RhSn/C	0.933	0.593	This work
Rh ₂ Sb NBs	0.506	0.462	5
Rh-Rh ₂ O ₃ -NPs/C	0.425	0.119	6
Rh ₂ P nanoparticles	0.65	0.52	7
Rh@Pt _{0.83} NBs	/	0.214 (1.0 M KOH)	8
Rh NP/PC	0.164	0.163	9
PdCu/C-200 °C	0.0156	0.011	10
PdCu/C-500 °C	0.2159	0.127	
Pd/C	0.0607	0.038	
Pt/C	0.1842	0.082	11
0.38 CeO _x -Pd/C	0.118	0.052	
Pd/C	0.045	0.021	
PtRu/Mo ₂ C	0.13	0.186	12
PtRu/Mo ₂ C-TaC	0.20	0.291	
PtRu/Mo ₂ C-W ₂ C	0.15	0.181	
Ir ₃ Pd ₁ Ru ₆ /C	0.6	0.73	13
Ir ₉ Pd ₁ /C	0.9	0.82	
Ir/O-MoO ₂	1.96	0.457	14
Pt ₆ NCs/C	1.546	0.646	15

Pt/C _{com}	0.351	0.113	
Pd ₃ Co@Pt/C	0.570	0.685	16

Table S4. The HOR activities of Rh/C, RhSn_{0.35}/C, RhSn_{0.51}/C (RhSn/C) and RhSn_{0.66}/C via the linear fitting.

Catalysts	$j^{0,s}$ (mA cm _{ECSA} ⁻²)	$j^{0,m}$ (mA μg _{PGM} ⁻¹)
Rh/C	0.489	0.216
RhSn _{0.35} /C	0.534	0.422
RhSn_{0.51}/C (RhSn/C)	0.852	0.509
RhSn _{0.66} /C	0.624	0.357

Table S5. The Mulliken charge and Hirshfeld charge in RhSn unit cell.

Atoms	Mulliken charge (e)	Hirshfeld charge (e)
Rh	-0.28	-0.02
Rh	-0.28	-0.02
Rh	-0.28	-0.02
Sn	0.84	0.06

Table S6. The bond lengths of Rh-O in RhSn and Rh shown in Figure S24.

Bonds	RhSn	Rh
Rh1-O	2.235	2.275
Rh2-O	2.239	2.362
Rh3-O	2.236	2.341

References

- 1 J. P. Perdew, K. Burke and M. Ernzerhof, *Phys. Rev. Lett.*, 1996, **77**, 3865-3868.
- 2 D. Vanderbilt, *Phys. Rev. B*, 1990, **41**, 7892-7895.
- 3 J. K. Norskov, T. Bligaard, A. Lagadottir, J. R. Kitchin, J. G. Chen, S. Pandeloy and U. Stimming, *J. Electrochem. Soc.*, 2005, **152**, J23-J26.
- 4 M. Kolb, F. Calle-Vallejo, L. B. F. Jurlink, M. T. M. Koper, *Chem. Phys.* 2014, **140**, 134708.
- 5 Y. Zhang, G. Li, Z. Zhao, L. Han, Y. Feng, S. Liu, B. Xu, H. Liao, G. Lu, H. L. Xin and X. Huang, *Adv. Mater.*, 2021, **33**, e2105049.
- 6 M. K. Kundu, R. Mishra, T. Bhowmik and S. Barman, *J. Mater. Chem. A*, 2018, **6**, 23531-23541.
- 7 F. Yang, X. Bao, D. Gong, L. Su, G. Cheng, S. Chen and W. Luo, *ChemElectroChem*, 2019, **6**, 1990-1995.
- 8 J. Cai, X. Liao, P. Li, Q. Wang, H. Huang, Z. Lyu, J. Lin and S. Xie, *Chem. Eng. J.*, 2022, **429**, 132414.
- 9 M. Ming, Y. Zhang, C. He, L. Zhao, S. Niu, G. Fan and J. S. Hu, *Small*, 2019, **15**, e1903057.
- 10 Y. Qiu, L. Xin, Y. Li, I. T. McCrum, F. Guo, T. Ma, Y. Ren, Q. Liu, L. Zhou, S. Gu, M. J. Janik and W. Li, *J. Am. Chem. Soc.*, 2018, **140**, 16580-16588.
- 11 R. K. Singh, E. S. Davydova, J. Douglin, A. O. Godoy, H. Tan, M. Bellini, B. J. Allen, J. Jankovic, H. A. Miller, A. C. Alba-Rubio and D. R. Dekel, *Adv. Funct. Mater.*, 2020, **30**, 2002087.
- 12 E. R. Hamo, R. K. Singh, J. C. Douglin, S. Chen, M. B. Hassine, E. Carbo-Argibay,

- S. Lu, H. Wang, P. J. Ferreira, B. A. Rosen and D. R. Dekel, *ACS Catal.*, 2021, **11**, 932-947.
- 13 H. Wang and H. D. Abruna, *J. Am. Chem. Soc.*, 2017, **139**, 6807-6810.
- 14 M. Li, Z. Xie, X. Zheng, L. Li, J. Li, W. Ding and Z. Wei, *ACS Catal.*, 2021, **11**, 14932-14940.
- 15 X. Wang, L. Zhao, X. Li, Y. Liu, Y. Wang, Q. Yao, J. Xie, Q. Xue, Z. Yan, X. Yuan and W. Xing, *Nat. Commun.*, 2022, **13**, 1596.
- 16 T. Zhao, Y. Hu, M. Gong, R. Lin, S. Deng, Y. Lu, X. Liu, Y. Chen, T. Shen, Y. Hu, L. Han, H. Xin, S. Chen and D. Wang, *Nano Energy*, 2020, **74**, 104877.